*J. Fluid Mech.* (2006), *vol.* 558, *pp.* 329–355.  
doi:10.1017/S0022112006009992 Printed in the United Kingdom

# Miscible displacements in Hele-Shaw cells: two-dimensional base states and their linear stability

By N. GOYAL AND E. MEIBURG†

Department of Mechanical Engineering, University of California, Santa Barbara, CA 93106, USA

(Received 20 June 2005 and in revised form 15 December 2005)

Miscible fingering in a Hele-Shaw cell is studied by means of Stokes simulations and linear stability analysis. The two-dimensional simulations of miscible displacements in a gap indicate the existence of a quasi-steady state near the tip of the displacement front for sufficiently large Péclet numbers and viscosity ratios, in agreement with earlier work by other authors. The front thickness of this quasi-steady state is seen to scale with $Pe^{-1/2}$, while it depends only weakly on the viscosity ratio. The nature of the viscosity–concentration relationship is found to have a significant influence on the quasi-steady state. For the exponential relationship employed throughout most of the investigation, we find that the tip velocity increases with $Pe$ for small viscosity ratios, while it decreases with $Pe$ for large ratios. In contrast, for a linear viscosity–concentration relationship the tip velocity is seen to increase with $Pe$ for all viscosity ratios. The simulation results suggest that in the limit of high $Pe$ and large viscosity contrast, the width and tip velocity of the displacement front asymptote to the same values as their immiscible counterparts in the limit of large capillary numbers.

In a subsequent step, the stability of the quasi-steady front to spanwise perturbations is examined, based on the three-dimensional Stokes equations. For all values of $Pe$, the maximum growth rate is found to increase monotonically with the viscosity ratio. The influence of $Pe$ on the growth of the instability is non-uniform. For mild viscosity contrasts, a larger $Pe$ is found to be destabilizing, while for large viscosity contrasts an increase in $Pe$ has a slightly stabilizing influence. A close inspection of the instability eigenfunction reveals the presence of two sets of counter-rotating roll-like structures, with axes aligned in the cross-gap and streamwise directions, respectively. The former lead to the periodic acceleration and deceleration of the front, while the latter result in the widening and narrowing of the front. These roll-like structures are aligned in such a way that the front widens where it speeds up, and narrows where it slows down. The findings from the present stability analysis are discussed and compared with their Darcy counterparts, as well as with experimental data by other authors for miscible and immiscible flows.

## 1. Introduction

The instability that forms when one fluid displaces another one of larger viscosity in a porous medium was first analysed half a century ago (Hill 1952; Saffman & Taylor

† Author to whom correspondence should be addressed: meiburg@engineering.ucsb.edu

1958; Chouke, Meurs & Poel 1959). In the decades since then, the viscous fingering instability has triggered a large body of experimental, theoretical and computational research (cf. reviews by Homsy 1987; Yortsos 1987) that sheds light on many of its fascinating facets. Its importance for practical applications such as oil recovery and hydrology, along with the central role it plays in the fundamental area of pattern formation, suggests that the exploration of the many remaining open issues will continue for years to come.

In the past, much of the theoretical and computational work on unstable miscible displacements has employed Darcy's law. Within this framework, Tan & Homsy (1986, 1987) investigate the linear stability of the flow as a function of the base flow concentration profile. They find that larger viscosity contrasts and steeper concentration fronts always result in higher growth rates and shorter wavelengths of the most dangerous mode. Corresponding results are obtained for vertical displacements with density stratification as well (Manickam & Homsy 1995). Similarly, Yortsos (1987) observes that in radial displacements both the most unstable and the cutoff wavenumbers scale linearly with the Péclet number of the flow. This destabilizing influence of larger Péclet numbers and viscosity contrasts is confirmed by nonlinear simulations of both rectilinear and radial displacements (Chen & Meiburg 1998; Ruith & Meiburg 2000 and references therein).

In contrast to these Darcy-based stability investigations, many experimental studies of viscous fingering have employed Hele-Shaw configurations, rather than 'true' porous media. The main reason for this approach lies in the ease with which the flow can be visualized in such apparatuses. In his classical set of experiments for vertically driven miscible interfaces, Wooding (1969) distinguishes the diffusively dominated short-time behaviour from its convectively dominated long-time counterpart. Paterson (1985) investigates the viscous fingering instability when water radially displaces glycerin in a horizontal geometry. For large Péclet numbers of $O(10^5)$, he observes a dominant wavelength of about four times the gap width. In downward displacements of a fluid by a lighter and less viscous one, Lajeunesse *et al.* (1997) find wavelengths closer to five times the gap width. These authors furthermore establish a critical velocity and viscosity ratio for a three-dimensional pattern to evolve.

It is well-known that the analogy between a true porous medium and a Hele-Shaw cell is incomplete (Homsy 1987), owing to the different nature of flow-induced dispersion effects in the two set-ups (Taylor 1953). Thus a comparison between Darcy results and Hele-Shaw experiments is not straightforward. To date, a closed-form description of dispersion in variable viscosity and density displacements within Hele-Shaw cells or porous media remains elusive. However, several attempts have been made to incorporate its effects into Darcy-based linear stability investigations, most of them based on the model of a passive tracer fluid (Taylor 1953). In this way, Tan & Homsy (1987) find a stabilizing influence of transverse dispersion. On the other hand, Yortsos & Zeybek (1988) observe a strongly destabilizing effect of longitudinal dispersion at high mobility ratios, which leads to an infinite short-wave cutoff wavelength in the limit of step-like base profiles. A similar approach towards modelling dispersive effects was taken in the nonlinear simulations by Petitjeans *et al.* (1999). Yang & Yortsos (1997), on the other hand, explicitly address Stokes flows in the Hele-Shaw geometry. They show by way of an asymptotic analysis that the approach of employing a convection–dispersion equation for the volume-averaged concentration is of limited value at high Péclet numbers. Yortsos & Zeybek (1988) also hint at the breakdown of this formalism as a plausible reason for the seemingly unphysical instability they observe for sharp base concentration profiles.

The above discussion reflects our currently incomplete understanding of the analogy between displacements in Hele-Shaw cells and porous media, respectively, with regard to a quantitative description of the miscible viscous fingering instability. The current investigation addresses this deficit by conducting two-dimensional Stokes flow simulations for plane channels, and by subsequently investigating the linear stability of the quasi-steady base states thus obtained with respect to spanwise perturbations. The resulting dispersion relations can then be compared with corresponding findings for Darcy flows, in order to identify both similarities and discrepancies between the two.

Earlier Stokes flow simulations for miscible displacements in plane channels are reported by Rakotomalala, Salin & Watzky (1997) for Péclet numbers up to $O(500)$, based on the BGK lattice Boltzmann approach. The authors identify parameter regimes in terms of Péclet number and mobility ratio for which a sharp concentration front develops. Their results compare well with the asymptotic predictions of Yang & Yortsos (1997). They also determine the shape of the displacement front in the limit of high mobility ratios, and they find good agreement with the results of Reinelt & Saffman (1985) for the corresponding case of immiscible displacements at high capillary numbers. In the present investigation, we will extend the results of Rakotomalala *et al.* (1997) to significantly higher Péclet numbers and mobility ratios, which will bring to light some new and unexpected effects.

However, the main goal of the present investigation lies in the systematic linear stability analysis of miscible displacements in Hele-Shaw cells, based on the three-dimensional Stokes equations. The nonlinear two-dimensional Stokes flow simulations merely serve to provide the quasi-steady base states required for this analysis. Our particular interest will focus on similarities and discrepancies between Stokes and Darcy results for the viscous fingering instability.

The paper is structured as follows. The physical problem, along with the governing equations and dimensionless parameters, is defined in § 2. Section 3 describes the results from the nonlinear Stokes simulations and provides a detailed characterization of the quasi-steady base states for the stability analysis. Section 4 discusses the subsequent linearization of the Stokes equations around this base state, along with the formulation of the numerical eigenvalue problem and the validation of the stability calculations. The results obtained from these calculations will be discussed in detail, with particular focus on the influence of the Péclet number and mobility ratio on the growth rate and the wavelength of the most dangerous mode. Differences between these findings and corresponding Darcy results will be discussed. Furthermore, comparisons with experimental data for Hele-Shaw displacements will be made, and similarities with immiscible displacements will be discussed. Finally, § 5 summarizes the main findings, and points to future research.

## 2. Physical problem

We consider two constant-density miscible fluids of different viscosities in a Hele-Shaw cell, as shown in figure 1. The less viscous fluid displaces the more viscous fluid to the right-hand side. For narrow gaps the flow velocities will be very small, so that the fluid motion is governed by the three-dimensional Stokes equations

$$\nabla \cdot \boldsymbol{u} = 0, \tag{2.1}$$

$$\nabla p = \nabla \cdot \boldsymbol{\tau}, \tag{2.2}$$

$$c_t + \boldsymbol{u} \cdot \nabla c = D\nabla^2 c. \tag{2.3}$$

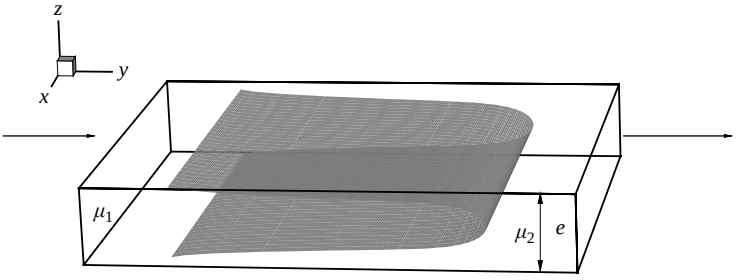


FIGURE 1. Geometry of the Hele-Shaw cell. The less viscous fluid on the left-hand side displaces the more viscous fluid on the right-hand side.

Here $\boldsymbol{u}$ denotes the flow velocity, and $c$ indicates the relative concentration of the more viscous fluid. $\boldsymbol{\tau} = \mu(\nabla u + \nabla u^T)$ represents the viscous stress tensor for Newtonian fluids. The components $\tau_{ij}$ have the usual definitions in Cartesian coordinates (Panton 1984). $D$ refers to the diffusion coefficient, which is assumed constant. The cell has a gap of width $e$, with $z$ indicating the gapwise or cross-gap direction. The $x$-direction will be referred to as the spanwise direction.

In following other authors, the viscosity $\mu$ is assumed to be an exponential function of the concentration $c$,

$$\mu = \mu_1 \mathrm{e}^{Rc}, \tag{2.4}$$

where $\mu_1$ indicates the viscosity of the less viscous fluid. The logarithm $R$ of the viscosity ratio is defined as

$$R = \ln \frac{\mu_2}{\mu_1}. \tag{2.5}$$

The governing equations are rendered dimensionless by introducing a characteristic length $L^*$, velocity $U^*$, time $T^*$ and pressure $P^*$ in the form of

$$L^* = e, \tag{2.6}$$

$$U^* = U, \tag{2.7}$$

$$T^* = \frac{e}{U}, \tag{2.8}$$

$$P^* = \frac{\mu_1 U}{e}. \tag{2.9}$$

where $U$ refers to the average velocity across the gap of the Hele-Shaw cell. We thus obtain the set of dimensionless equations as

$$\nabla \cdot \boldsymbol{u} = 0, \tag{2.10}$$

$$\nabla p = \nabla \cdot \boldsymbol{\tau}, \tag{2.11}$$

$$c_t + \boldsymbol{u} \cdot \nabla c = \frac{1}{Pe} \nabla^2 c, \tag{2.12}$$

where

$$Pe = \frac{Ue}{D}. \tag{2.13}$$

The Péclet number $Pe$ indicates the relative strength of convective to diffusive transport.

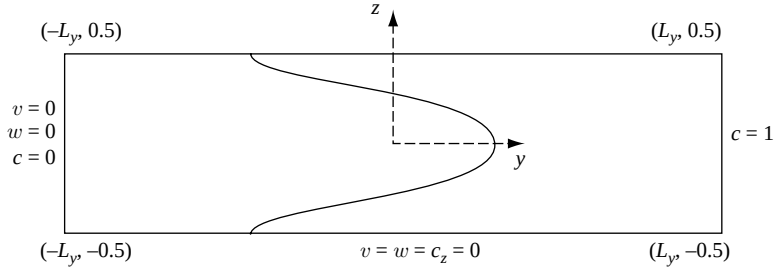


FIGURE 2. Coordinate system of the computational domain, with boundary conditions in terms of deviation velocities, as described in the text.

## 3. Two-dimensional Stokes flow simulations

### 3.1. *Numerical implementation*

Nonlinear Stokes flow simulations are employed to obtain the two-dimensional convectively dominated base state required for the subsequent linear stability analysis. For this purpose, we cast the two-dimensional Stokes equations into the fourth-order streamfunction formulation, by taking the curl of the momentum equations and using the definition of the streamfunction to replace the velocity terms by the streamfunction and its derivatives. We arrive at

$$\nabla^4\psi = F(y, z), \tag{3.1}$$

$$c_t + \boldsymbol{u}\cdot\nabla c = \frac{1}{Pe}\nabla^2 c, \tag{3.2}$$

where the streamfunction $\psi$ is defined by

$$v = \psi_z, \quad w = -\psi_y \tag{3.3}$$

and

$$\nabla^4\psi = \psi_{yyyy} + 2\psi_{yyzz} + \psi_{zzzz}, \tag{3.4}$$

$$\begin{aligned} F(y, z) = {} & R\left(c_{yy} + c_{zz} + Rc_y{}^2 - Rc_z{}^2\right)(\psi_{zz} - \psi_{yy}) - 4R(c_{yz} + Rc_yc_z)\psi_{yz} \\ & - 2Rc_y(\psi_{yyy} + \psi_{yzz}) - 2Rc_z(\psi_{yyz} + \psi_{zzz}). \end{aligned} \tag{3.5}$$

Figure 2 shows the two-dimensional computational domain employed for the simulations, along with the imposed boundary conditions. We select the size of the domain in the flow direction sufficiently large, so that a quasi-steady displacement front can evolve without being affected by the upstream and downstream boundaries. The overall velocity field is decomposed into plane Poiseuille flow plus a deviation from it, which goes to zero at all boundaries. We thus obtain the following set of boundary conditions for this deviation component

$$y = L_y: \qquad \psi = 0, \qquad \psi_y = 0, \qquad c = 1 \tag{3.6}$$

$$y = -L_y: \qquad \psi = 0, \qquad \psi_y = 0, \qquad c = 0 \tag{3.7}$$

$$z = \pm 0.5: \qquad \psi = 0, \qquad \psi_z = 0, \qquad c_z = 0 \tag{3.8}$$

We perform all simulations in a reference frame moving with the average velocity of the Poiseuille flow and employ a domain of length 8 for most simulations.

The temporal discretization is accomplished by an explicit third-order accurate, low-storage Runge–Kutta (Wray 1991) time integration scheme for updating the concentration field. Compact finite differences (Lele 1992) of up to sixth order in

the interior of the domain, and fourth order at the boundaries, are employed for the spatial discretization of the concentration derivatives, in order to avoid the appearance of numerical instabilities in the convection–diffusion equation. As will be seen below, a sharp concentration front evolves at the tip of the displacement front, particularly at high values of $Pe$, while the velocity fields are far smoother. Hence second-order finite differences are sufficient for discretizing the streamfunction derivatives in both directions. This lower-order approximation also helps keep the coefficient matrix for the discretized fourth-order streamfunction equation sparse, so that it can be solved by means of the sparse direct linear solver implemented in the software package UMFPACK (Davis & Duff 1997; Davis 2003*a*, *b*). The largest simulations involved a computational domain of length 10 in the streamwise direction, with $1281 \times 225$ grid points.

We examined the influence of the domain length and spatial resolution on our results, in order to ensure the absence of any numerical artefacts in our simulation results with regard to the detailed shape of the front tip and its propagation velocity. We validated our code by such simple test cases as the one-dimensional self-similar diffusion of the initial concentration profile in the absence of flow, and the reproduction of plane channel flow across the gap of the cell when the viscosities of the two fluids are equal. Additionally, we applied our nonlinear simulation procedure to calculate the growth rates of gravity-driven instabilities in miscible Hele-Shaw flows, for which we had derived linear stability results in a previous investigation cf. (Goyal & Meiburg 2004). Excellent agreement between these two cases validated our numerical results. Over the next few sections we also compare our findings with some earlier results in literature, in different parameter regimes, which provides further validation.

### 3.2. *Evolution of the quasi-steady displacement front*

Figure 3 depicts concentration fields from a numerical simulation for $Pe = 10^3$ and $R = 3$ at various times. The initial condition specifies a one-dimensional profile for the concentration, along with plane Poiseuille flow for the velocity field. The concentration profile is taken from the family of one-dimensional solutions describing the self-similar diffusive decay of a step profile

$$c_0 = \tfrac{1}{2} + \tfrac{1}{2}\mathrm{erf}\left(\frac{y}{\delta}\right). \tag{3.9}$$

The initial profile thickness is governed by the thickness parameter $\delta$. Results from simulations for different values of $\delta$ demonstrate that the final quasi-steady shape of the front is independent of $\delta$, so that we can employ a value of $\delta = 0.1$ for all calculations. Upon the start of the flow, the velocity field immediately deforms the concentration distribution in the interior of the cell, while the concentration at the wall changes due to diffusion only. In turn, this change in the concentration distribution modifies the viscosity field, thus leading to the formation of a well-defined displacement front of the less viscous fluid, which propagates along the centre of the Hele-Shaw cell. This front exhibits a steep concentration layer at the tip, and diffusively spreading layers at its sides. After some time, the tip of the front and the associated concentration field reach a quasi-steady state in the reference frame moving with the front.

We now discuss the properties of this quasi-steady displacement front in more detail. In order to establish the existence of this quasi-steady state quantitatively, we define the front thickness $d$ as the distance in the horizontal direction over which the concentration at the tip of the front changes from 0.1 to 0.9 (cf. figure 4*a*).

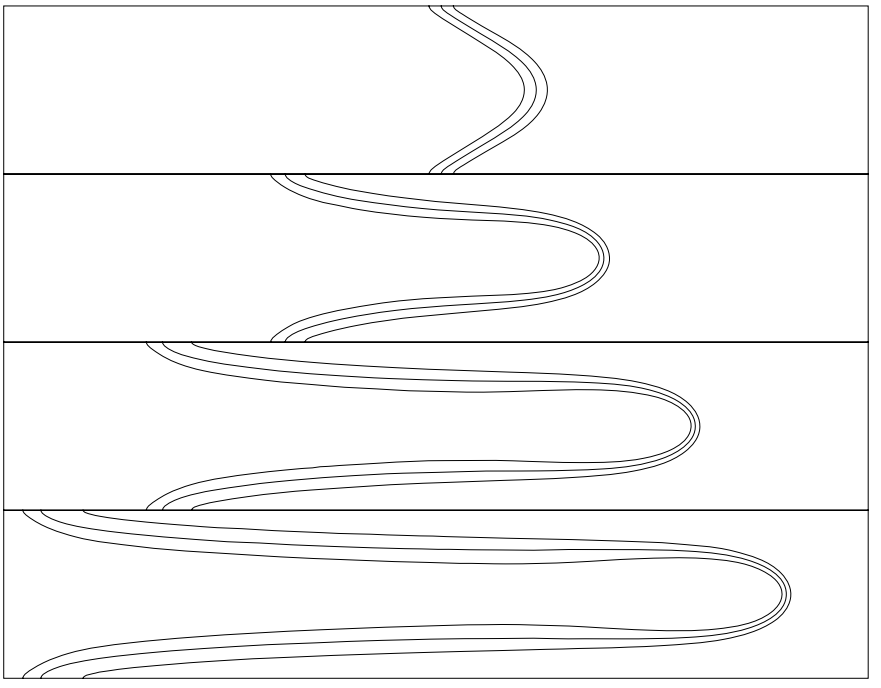

FIGURE 3. Evolution of a quasi-steady base state in the area near the tip of the displacement front for $Pe = 10^3$ and $R = 3$. The $c = 0.1$, 0.5 and 0.9 contours are plotted at $t = 0.5$, 1.5, 2.5 and 3.5, respectively.

Figure 4(*b*) plots $d$ *vs.* time, where the $c = 0.1$ and 0.9 locations have been determined to a high degree of accuracy by means of a cubic spline interpolation of the computed concentration field. It can be seen that for both of the initial interface thickness parameters, $d$ attains the same constant value for large times. We denote this final constant value of the front thickness by $d_0$. This behaviour demonstrates the emergence of a quasi-steady state whose properties do not depend on the initial interfacial thickness parameter $\delta$, as mentioned earlier. Corresponding results are generally obtained for Péclet numbers above $O(500)$ and viscosity contrasts of $R = 3$ and higher. For smaller $Pe$ and $R$ values, strong diffusive effects prevent the evolution of a quasi-steady state. Here diffusion outweighs convection, so that a steep concentration layer at the tip of the front cannot be maintained.

Figure 5 shows the value of the quasi-steady front thickness for various Péclet numbers and viscosity ratios. We remark that for either $R < 2$ or $Pe < 500$, truly quasi-steady states do not form, while for $R = 2$ a quasi-steady state is reached only for $Pe > 2000$. However, for comparison purposes, the figure still displays results for several lower values of $Pe$ and $R = 2$, since a nearly steady state does persist for a very short period of time. As $Pe$, and hence the convective effects, increase, the front thickness is seen to diminish. Basic scaling arguments in terms of dimensional quantities explain this behaviour, cf. the work by Chen & Meiburg (1996) on miscible displacements in capillary tubes. A straightforward one-dimensional balance of strain and diffusion effects on the quasi-steady concentration field near the tip of the front according to

$$v\frac{\partial c}{\partial y} = D\frac{\partial^2 c}{\partial y^2}, \tag{3.10}$$

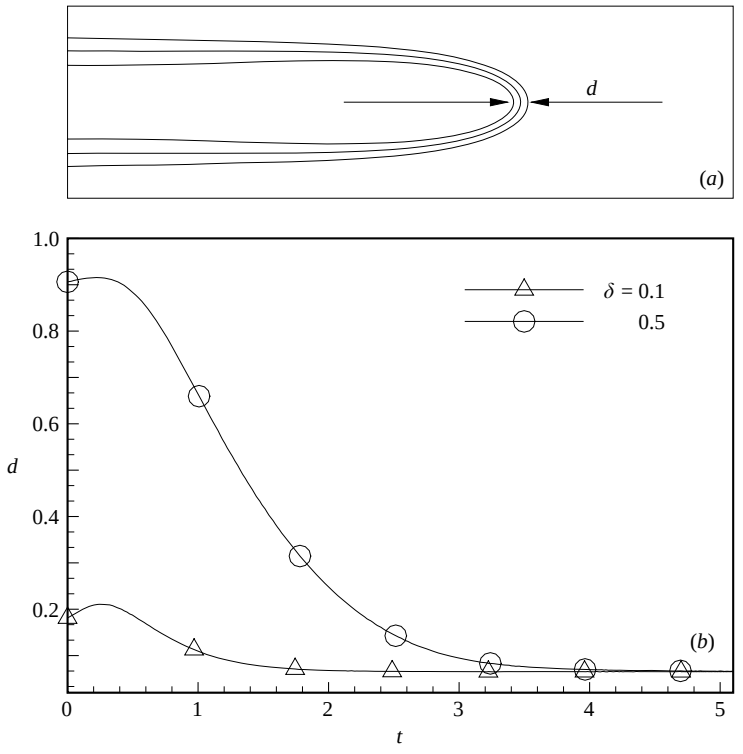


FIGURE 4. (*a*) The front thickness $d$ is defined as the horizontal distance between the $c = 0.1$ and 0.9 contours along $z = 0$. (*b*) $d$ *vs.* time for $Pe = 10^3$, $R = 3$ and two different initial interface thickness parameters $\delta$. Note that the final value $d = d_0$ is independent of the initial value of $\delta$.

yields for the quasi-steady front thickness $d_0$

$$d_0 \backsim Pe^{-1/2}. \tag{3.11}$$

Thus, the front thickness should scale inversely with the square root of $Pe$. Figure 5 confirms the validity of this relationship, which holds with a high degree of accuracy for $R > 3$. Eventually, the quasi-steady state will decay for all Péclet numbers, owing to lateral diffusion of the more viscous fluid into the front. Chen & Meiburg (1996) also provide scaling arguments similar to the above for the length of the time intervals over which this steady state persists for different Péclet numbers. The numerical expense associated with these simulations prevents us from verifying the validity of these scaling arguments, since we cannot perform simulations over such long periods of time.

Rakotomalala *et al.* (1997) performed corresponding BGK lattice gas simulations for miscible displacements up to $Pe = 512$. In this range of Péclet numbers, and for viscosity ratios of up to $R = 7$, the present Stokes simulation results compare well with their earlier calculations. To avoid repetition, we hence do not present any results for Péclet numbers smaller than $O(500)$, and instead refer the reader to their work. Specifically, they provide data on the tip velocity, the fraction of fluid left behind on the walls of the cell, and the reduced finger width. Our simulations confirm these results. In the following, we will report several new observations for higher values of

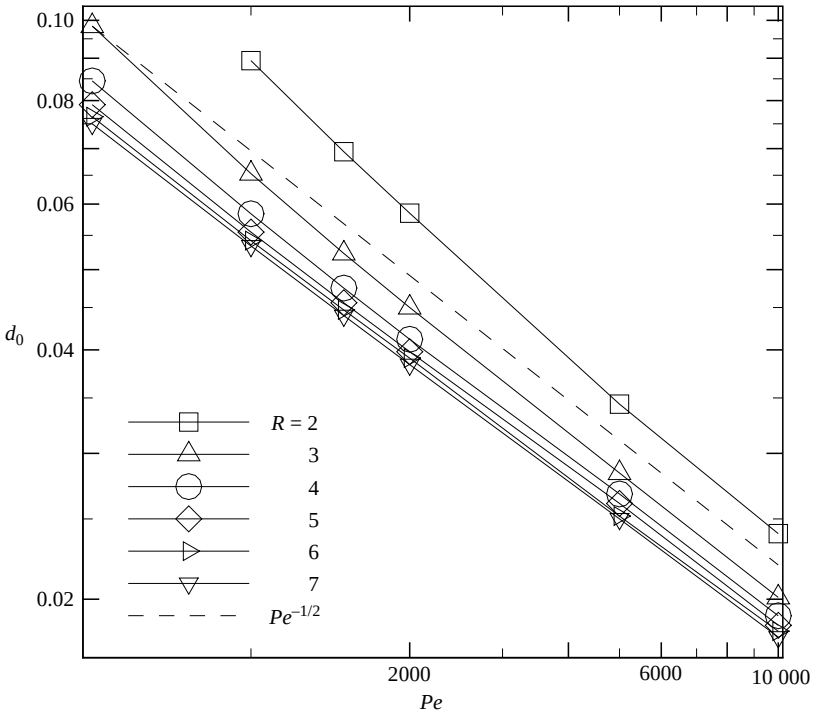


FIGURE 5. Thickness of the quasi-steady displacement front as a function of $Pe$ for different viscosity ratios. The dashed line corresponds to the $Pe^{-1/2}$ power law.

$Pe$ and large viscosity contrasts that cannot be inferred from the earlier, lower $Pe$ results.

### 3.3. *Velocity of the displacement front*

Figure 6($a$) displays the velocity of the quasi-steady tip as a function of the Péclet number for different viscosity ratios. We noted earlier that our simulations are performed in a reference frame moving with the average velocity of the Poiseuille flow. However, in all our figures we include the contribution from the mean flow and present the total velocity of the front. At $R = 2$ the velocity of the tip increases with $Pe$, while for $R = 3$ an intermediate Péclet number of 1000 corresponds to a maximum in the tip velocity. Here it is to be kept in mind that these results for low $Pe$ and $R$ are not yet truly quasi-steady, as discussed above. On the other hand, for higher viscosity contrasts we find the tip velocity to decrease with increasing $Pe$. This observation is in contrast to, for example, the results reported by Petitjeans & Maxworthy (1996) for miscible displacements in capillary tubes, which exhibit an increase in the tip velocity with increasing $Pe$. Corresponding data for immiscible displacements (cf. Reinelt & Saffman (1985) for Hele-Shaw flows; Taylor (1961) and Cox (1962) for capillary tubes) typically show an increase in tip velocity with capillary number $Ca$, which is defined as

$$Ca = \frac{\mu U}{T}. \tag{3.12}$$

Here $T$ refers to the surface tension, while $\mu$ and $U$ have their usual definitions provided earlier. We will return below to this interesting result regarding the $Pe$-dependence of the tip velocity.

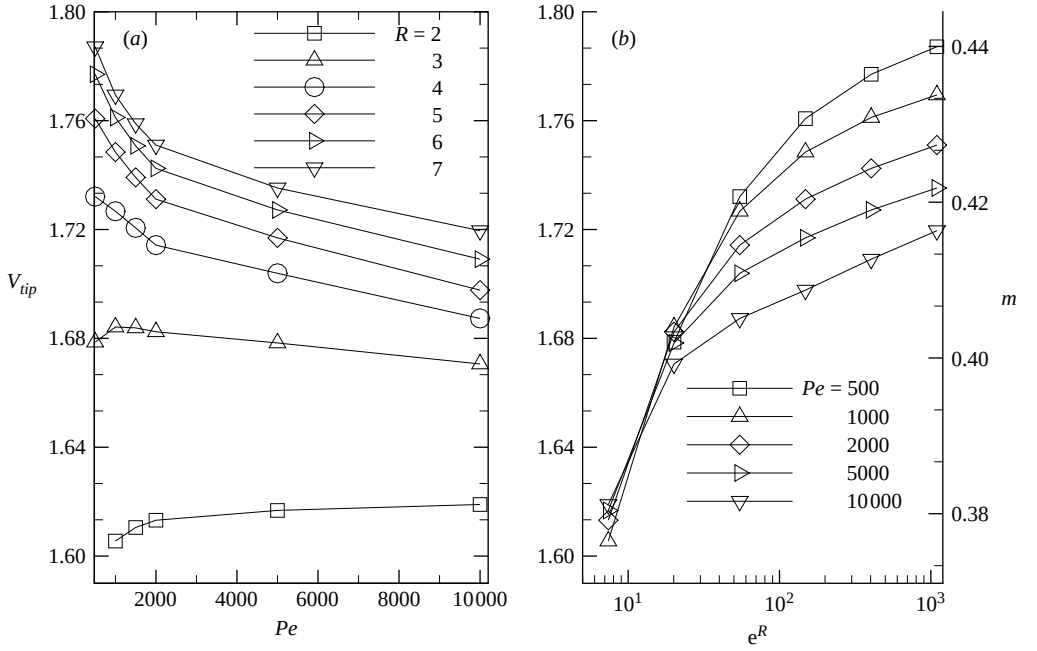


FIGURE 6. Quasi-steady tip velocity as a function of (*a*) *Pe*, and (*b*) *R*. For low values of *R*, the front velocity increases with *Pe*, while the opposite holds for large values of *R*. At mild viscosity contrasts, the tip velocity is nearly independent of *Pe*, while for larger viscosity ratios the front slows down as *Pe* increases.

Figure 6(*b*) shows the variation of the tip velocity with the exponential of the viscosity ratio $e^R$, in order to facilitate comparison with the results of Rakotomalala *et al.* (1997). The secondary axis depicts the fraction *m* of the more viscous fluid left behind on the walls of the cell. This fraction *m*, defined as

$$m = 1 - \frac{U}{V_{tip}}, \tag{3.13}$$

is frequently employed as a diagnostic measure in both capillary tubes and Hele-Shaw cells. For all values of *Pe*, an increase in the viscosity contrast results in a faster tip, and hence a larger value of *m*. The same trend was observed by Rakotomalala *et al.* (1997) for *Pe* up to 512. At a value of $Pe = 500$, our results for the tip velocity and *m* duplicate their values almost exactly over the range of viscosity ratios (cf. figure 10 in Rakotomalala *et al.* 1997). As mentioned earlier and shown in figure 6(*a*), the behaviour at higher *Pe* cannot be extrapolated from these lower *Pe* results, owing to the changes in the dependence of $V_{tip}$ on *Pe*.

Yang & Yortsos (1997) propose an asymptotic method for analysing two-dimensional Hele-Shaw flows in the limits of infinite Péclet number and large aspect ratio. Under these conditions, the flow away from the tip reduces to a parallel flow between two plates, and it can be described by a conservation equation for the gap-averaged concentration. Lajeunesse *et al.* (1999) used the same approach to include buoyancy effects for vertical Hele-Shaw cells or tubes. They analyse the resulting hyperbolic equation using kinematic wave theory. Under these assumptions the gap-averaged version of (2.12) takes the form

$$\frac{\partial \bar{C}(y,t)}{\partial t} + \frac{\partial F(y,t)}{\partial y} = 0, \tag{3.14}$$

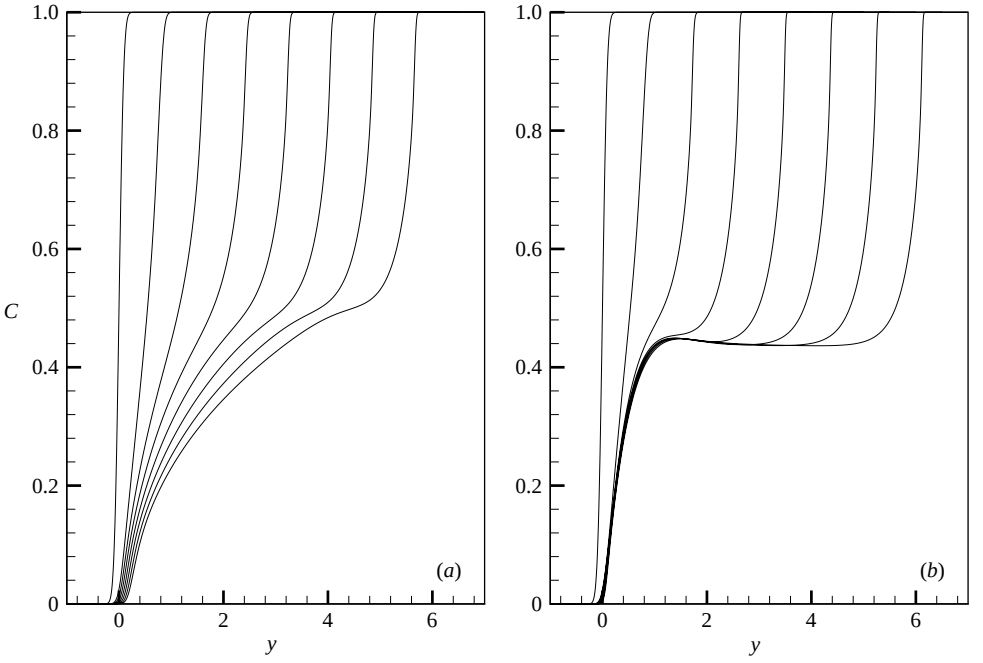


FIGURE 7. Simulation data for the gap-averaged concentration as a function of the streamwise distance at $t = 0, 0.5, 1.0 \ldots 3.5$, for $Pe = 2000$ and (*a*) $R = 2$, (*b*) $R = 7$.

where

$$\bar{C}(y,t) = \int_{-0.5}^{0.5} c(y,z,t)\,\mathrm{d}z, \tag{3.15}$$

$$F(y,t) = \int_{-0.5}^{0.5} c(y,z,t)v(y,z,t)\,\mathrm{d}z, \tag{3.16}$$

are the gap-averaged concentration and the mass flux of the more viscous fluid, respectively. Thus the convective velocity of each concentration value $\bar{C}$ depends on the shape of the flux function $F\left(\bar{C}\right)$ and is given by

$$V(\bar{C}) = \frac{\mathrm{d}F}{\mathrm{d}\bar{C}}. \tag{3.17}$$

A closed-form expression for the streamwise velocity component can then be derived as a function of the specific viscosity–concentration relationship. By assuming a step profile for the viscosity across the interface, the above authors obtain explicit expressions for the flux function $F\left(\bar{C}\right)$ in terms of the viscosity ratio and $\bar{C}$. In our case, both the Péclet number and the aspect ratio are finite, and the viscosity varies exponentially with the concentration. Nevertheless, for large $Pe$ the analysis should still be approximately applicable, and it is of interest to check if it can predict the tip velocities observed in the present investigation.

Figure 7 displays the concentration field averaged across the gap as a function of the streamwise coordinate for $Pe = 2000$, and $R = 2$ and 7. Figures 8(*a*) and 8(*b*) plot the flux $F$ as a function of $\bar{C}$, and $\bar{C}$ as a function of $V(\bar{C})$, for $Pe = 2000$ and various $R$. A truly quasi-steady state does not evolve for $R = 2$ and there is a smooth change in the average concentration from 0 to 1. On the other hand, for the higher viscosity contrast near $\bar{C} = 0.45$, the average concentration increases and

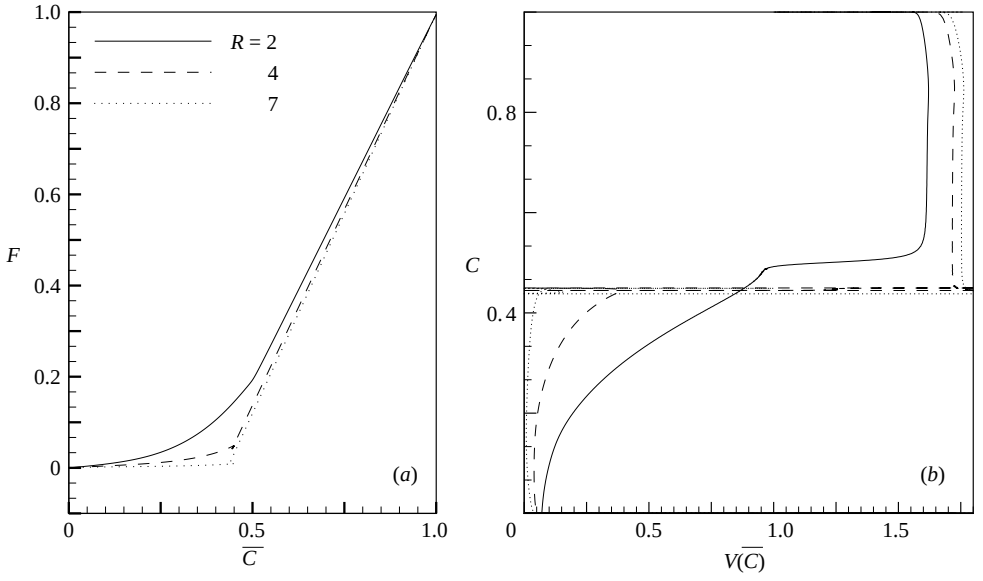


FIGURE 8. (*a*) Flux, and (*b*) velocity of the gap-averaged concentration value as a function of the gap-averaged concentration, for $Pe = 2000$ and different viscosity ratios.

then decreases in the streamwise direction, before finally increasing rapidly to unity, as shown in figure 7(*b*). This is a result of the bulging of the finger just behind the tip, which becomes more pronounced with an increasing viscosity contrast. It is already visible for $R = 3$ in figure 3. This is responsible for the decrease in the average concentration with $y$ behind the tip as mentioned above. Consequently, $F$ becomes double-valued at higher viscosity contrasts, near $\bar{C} = 0.45$, cf. figure 8(*a*). As a result of this discontinuity, the flux function ceases to be differentiable in the region near $\bar{C} = 0.45$ and the fitting procedure assigns an infinite value to the velocity in figure 8(*b*). However, it can be seen that for all higher $\bar{C}$ the velocity is nearly constant, until it is slightly reduced as it approaches the pure more viscous fluid. This constant plateau value represents the velocity of the moving tip. Our results correspond to the case for which Lajeunesse *et al.* (1999) observe three-dimensional patterns in their experiments, along with a frontal shock with a velocity greater than the maximum Poiseuille flow velocity of 1.5. The present flux values and velocities of the shock compare well with their predictions. Note that our plots appear inverted with respect to theirs, since we define our concentration based on the more viscous fluid. Of course this is purely a qualitative comparison, owing to the presence of gravitational effects in the experiments.

Figure 9 compares the velocities obtained from figure 8 with those from our simulations over the entire parameter regime. We observe excellent agreement between the two sets of results. As $Pe$ increases, the agreement between theoretical predictions and simulation results improves, since the underlying assumptions hold more rigorously at higher Péclet numbers. Thus, at $Pe = 10\,000$ the tip velocity derived from the kinematic wave theory is nearly identical to the simulation result.

### 3.4. *Influence of the viscosity–concentration relationship*

For different fluid pairs, the dependence of the viscosity on the concentration can be of different functional form. In order to evaluate the influence of the specific

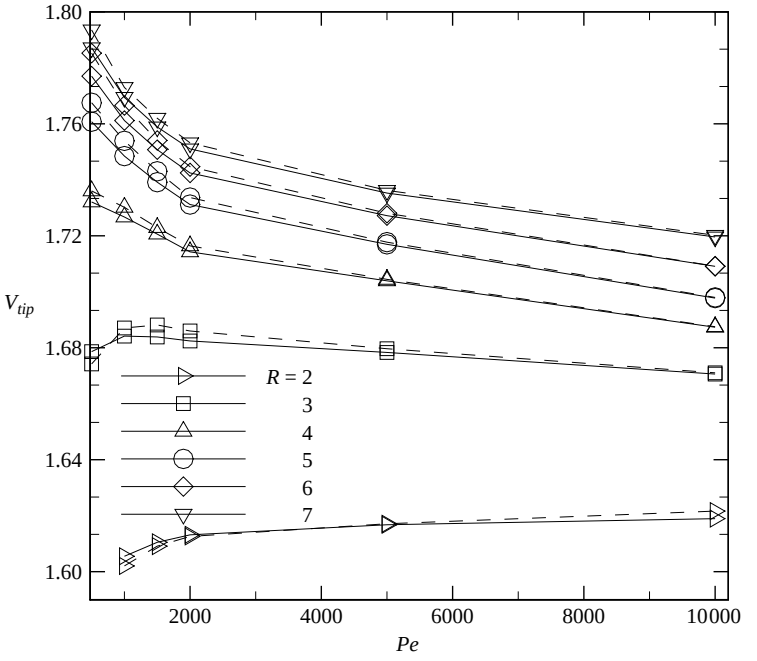


FIGURE 9. Quasi-steady tip velocity as a function of *Pe*, for different viscosity ratios. Comparison of the present simulation data with kinematic wave theory results. Solid lines: present simulation data. Dashed lines correspond to the tip velocity obtained from $V(\bar{C}) = \mathrm{d}F/\mathrm{d}\bar{C}$.

viscosity–concentration relationship, we perform an additional set of simulations for a linear dependence of the viscosity on the concentration

$$\mu = 1 + (\mathrm{e}^R - 1)c, \tag{3.18}$$

with $R = 7$ and different values of *Pe*. Figure 10(*a*) shows that the front is slightly thicker if the viscosity varies linearly with the concentration, while it follows the same overall trend of decreasing width with increasing *Pe*. For larger *Pe* this difference decreases, as the concentration boundary layer becomes very thin. On the other hand, the tip velocity is much more sensitive to the specific viscosity–concentration relationship. For a linear dependence, the tip is seen to move faster for larger *Pe*, while it slows down for an exponential dependence. For large *Pe* values, the tip velocities converge to the same asymptotic value, while for lower Péclet numbers of $O(1000)$ the difference in the front velocities can be up to 5 %. This could in part explain the discrepancies observed for capillary tube displacements between the experimental data of Petitjeans & Maxworthy (1996) and the corresponding simulation results of Chen & Meiburg (1996) for the fraction of the more viscous fluid left behind on the walls.

### 3.5. *Comparison with earlier miscible and immiscible results*

As mentioned earlier, immiscible displacements have been studied in some detail in the past, both experimentally and numerically. It is thus interesting to compare miscible displacements in the limit of large *Pe* with immiscible displacements in the limit of large *Ca*. For this purpose we focus on the width of the displacement front,

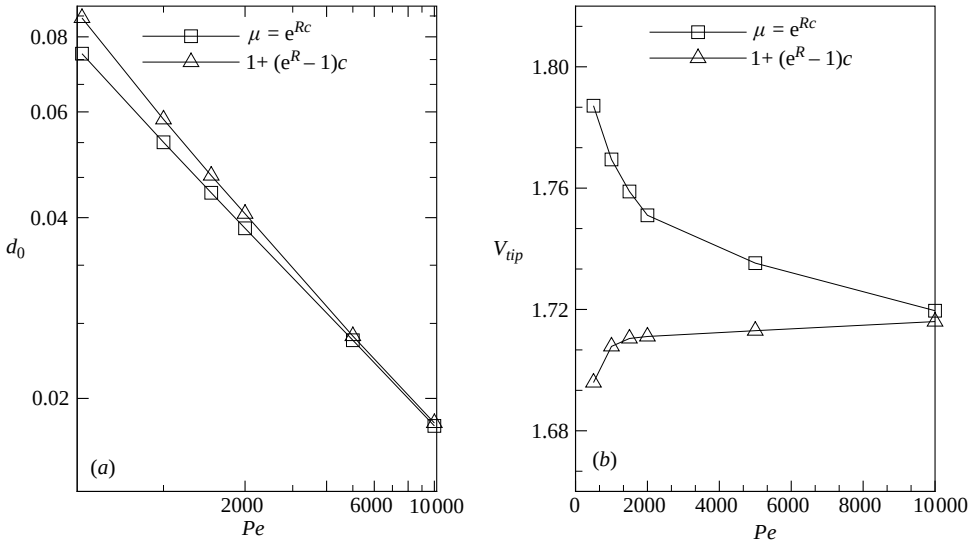


FIGURE 10. Influence of the viscosity–concentration relationship for $R = 7$ on (*a*) the front thickness and (*b*) the tip velocity of the displacement front. With regard to the front thickness, the influence is seen to be rather small. For the linear dependence, the tip moves faster as *Pe* increases, whereas for the exponential form, the tip slows down.

commonly referred to as the reduced finger width, which is defined as

$$\lambda = 1 - m \quad \text{Hele-Shaw cell,} \tag{3.19}$$

$$\lambda = \sqrt{1 - m} \quad \text{capillary tube.} \tag{3.20}$$

Reinelt & Saffman (1985) solve the Stokes equations numerically for immiscible fluid displacements in a Hele-Shaw cell or capillary tube, in the limit of $R \to \infty$. Their results show that as *Ca* increases to 2, the reduced finger width $\lambda$ asymptotes to a value of about 0.62. Analogously, in a capillary tube, Taylor (1961) measured $\lambda = 0.67$ for $Ca = 2$. Cox (1962) performed experiments at much higher values $Ca > 10$ and showed that $\lambda$ asymptotes to 0.63. The miscible fluid capillary-tube experiments by Petitjeans & Maxworthy (1996) with $R \sim 5$ and *Pe* of $O(40\,000)$ asymptote to the same value of the reduced finger width. In these experiments, $\lambda$ decreases with increasing *Pe*, while our simulations demonstrate an increase in $\lambda$ with *Pe*. This is because of the exponential viscosity–concentration relationship employed by us, since the finger width is merely the reciprocal of the quasi-steady tip velocity of the displacement front.

Figure 11 displays the reduced finger width from our simulations as a function of *R* for different *Pe*. We also plot the asymptotic limit of Reinelt & Saffman (1985) for high *Ca* and $R \to \infty$ in figure 11. It is clear that a further increase in *Pe* would cause the finger width to approach the limit given by Reinelt & Saffman (1985).

## 4. Linear stability analysis

### 4.1. *Formulation of the eigenvalue problem*

In the following, we investigate the linear stability of the quasi-steady two-dimensional base state with regard to periodic spanwise perturbations. Towards this end, the three-dimensional Stokes equations are linearized around the two-dimensional base

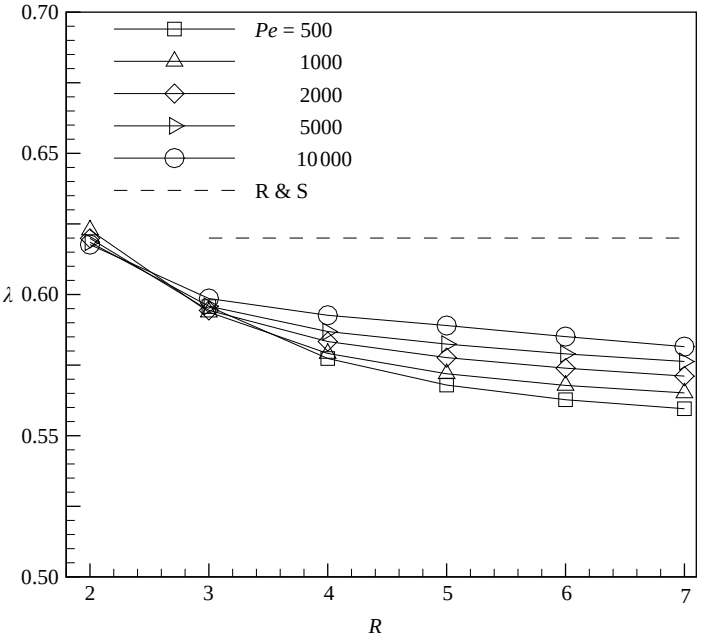


FIGURE 11. Reduced finger width $\lambda$ *vs*. $R$ for different $Pe$. The dashed line (R&S) corresponds to the immiscible results of Reinelt & Saffman (1985) for large $Ca$ in the limit of $R \to \infty$.

state

$$u(x, y, z, t) = 0 + \hat{u}(y, z)\sin(\beta x)\,\mathrm{e}^{\sigma t}, \tag{4.1}$$

$$v(x, y, z, t) = \bar{v}(y, z) + \hat{v}(y, z)\cos(\beta x)\,\mathrm{e}^{\sigma t}, \tag{4.2}$$

$$w(x, y, z, t) = \bar{w}(y, z) + \hat{w}(y, z)\cos(\beta x)\,\mathrm{e}^{\sigma t}, \tag{4.3}$$

$$p(x, y, z, t) = \bar{p}(y, z) + \hat{p}(y, z)\cos(\beta x)\,\mathrm{e}^{\sigma t}, \tag{4.4}$$

$$c(x, y, z, t) = \bar{c}(y, z) + \hat{c}(y, z)\cos(\beta x)\,\mathrm{e}^{\sigma t}. \tag{4.5}$$

Here, variables marked with a hat represent two-dimensional eigenfunctions, while those marked with an overbar denote the base state. Note that the perturbations are assumed to be wavelike in the spanwise $x$-direction. The above expressions are substituted into the governing equations, the base state is subtracted out, and all terms quadratic in the disturbances are neglected.

The resulting set of equations is discretized in a domain that extends from $z = -0.5$ to 0.5 and is centred around the tip of the displacement front in the streamwise direction. This domain has to be taken sufficiently large, so that the perturbations can be assumed to vanish at the upstream and downstream boundaries. At the walls, the perturbation velocity is set to zero, and the normal derivative of the concentration perturbation is assumed to vanish. We do not require boundary conditions for the pressure perturbation. The base state velocity and concentration fields as well as all their necessary derivatives are interpolated from the DNS grid to the stability grid using sixth-order Lagrangian interpolation. Since large gradients in both directions exist near the tip of the displacement front, we follow the approach outlined by Vanaparthy, Meiburg & Wilhelm (2003) in order to concentrate the grid points around the tip of the front. In the $z$-direction, the nodes are spaced equidistantly, while a stretched grid is employed on the two subdomains $y \geqslant y_{tip}$ and $y \leqslant y_{tip}$ which

concentrates the grid points near $y_{tip}$. For this purpose, a mapping function provided by Fletcher (1990) is employed

$$y_i = s_i \frac{l}{2}, \tag{4.6}$$

where

$$s_i = P\eta_i + (1-P)\left(1 - \frac{\tanh[Q(1-\eta_i)]}{\tanh Q}\right), \tag{4.7}$$

with

$$\eta_i = \frac{i-1}{n-1}. \tag{4.8}$$

Here $n$ represents the number of axial points within each subdomain, while $P$ and $Q$ are parameters to be chosen appropriately, in order to obtain a suitable distribution of grid points. Thus discretization of the equations using second-order central finite-differencing in both directions, yields an algebraic system of the form

$$\boldsymbol{A}\,\boldsymbol{\phi} = \sigma\,\boldsymbol{B}\,\boldsymbol{\phi}. \tag{4.9}$$

This represents a generalized eigenvalue problem with the growth rate $\sigma$ as the eigenvalue, while the eigenvector $\phi$ reflects the shape of the perturbations. As usual, a positive (negative) eigenvalue indicates unstable (stable) behaviour. $\boldsymbol{A}$ and $\boldsymbol{B}$ denote the coefficient matrices and are given by

$$\boldsymbol{A} = \begin{pmatrix} \boldsymbol{0} & \beta\boldsymbol{I} & \boldsymbol{\partial}_y & \boldsymbol{\partial}_z & \boldsymbol{0} \\ \beta\boldsymbol{I} & \boldsymbol{M}_1 & \boldsymbol{M}_2 & \boldsymbol{M}_3 & \boldsymbol{0} \\ -\boldsymbol{\partial}_y & \boldsymbol{0} & \boldsymbol{M}_4 & \boldsymbol{M}_5 & \boldsymbol{M}_6 \\ -\boldsymbol{\partial}_z & \boldsymbol{0} & \boldsymbol{M}_7 & \boldsymbol{M}_8 & \boldsymbol{M}_9 \\ \boldsymbol{0} & \boldsymbol{0} & -\bar{\boldsymbol{c}}_y & -\bar{\boldsymbol{c}}_z & \boldsymbol{M}_{10} \end{pmatrix}, \tag{4.10}$$

with

$$\boldsymbol{M}_1 = \mathrm{e}^{R\bar{c}}[-\beta^2\boldsymbol{I} + \boldsymbol{\partial}_{yy} + \boldsymbol{\partial}_{zz} + R(\bar{c}_y\boldsymbol{\partial}_y + \bar{c}_z\boldsymbol{\partial}_z)], \tag{4.11}$$

$$\boldsymbol{M}_2 = -\beta R\mathrm{e}^{R\bar{c}}\bar{c}_y\boldsymbol{I}, \tag{4.12}$$

$$\boldsymbol{M}_3 = -\beta R\mathrm{e}^{R\bar{c}}\bar{c}_z\boldsymbol{I}, \tag{4.13}$$

$$\boldsymbol{M}_4 = \mathrm{e}^{R\bar{c}}[-\beta^2\boldsymbol{I} + \boldsymbol{\partial}_{yy} + \boldsymbol{\partial}_{zz} + R(2\bar{c}_y\boldsymbol{\partial}_y + \bar{c}_z\boldsymbol{\partial}_z)], \tag{4.14}$$

$$\boldsymbol{M}_5 = R\mathrm{e}^{R\bar{c}}\bar{c}_z\boldsymbol{\partial}_y, \tag{4.15}$$

$$\boldsymbol{M}_6 = R\mathrm{e}^{R\bar{c}}[2\bar{v}_y(R\bar{c}_y\boldsymbol{I} + \boldsymbol{\partial}_y) + (\bar{v}_z + \bar{w}_y)(R\bar{c}_z\boldsymbol{I} + \boldsymbol{\partial}_z) + (\bar{v}_{yy} + \bar{v}_{zz})\boldsymbol{I}], \tag{4.16}$$

$$\boldsymbol{M}_7 = R\mathrm{e}^{R\bar{c}}\bar{c}_y\boldsymbol{\partial}_z, \tag{4.17}$$

$$\boldsymbol{M}_8 = \mathrm{e}^{R\bar{c}}[-\beta^2\boldsymbol{I} + \boldsymbol{\partial}_{yy} + \boldsymbol{\partial}_{zz} + R(\bar{c}_y\boldsymbol{\partial}_y + 2\bar{c}_z\boldsymbol{\partial}_z)], \tag{4.18}$$

$$\boldsymbol{M}_9 = R\mathrm{e}^{R\bar{c}}[2\bar{w}_z(R\bar{c}_z\boldsymbol{I} + \boldsymbol{\partial}_z) + (\bar{v}_z + \bar{w}_y)(R\bar{c}_y\boldsymbol{I} + \boldsymbol{\partial}_y) + (\bar{w}_{yy} + \bar{w}_{zz})\boldsymbol{I}], \tag{4.19}$$

$$\boldsymbol{M}_{10} = \frac{1}{Pe}(-\beta^2\boldsymbol{I} + \boldsymbol{\partial}_{yy} + \boldsymbol{\partial}_{zz}) - \bar{v}\boldsymbol{\partial}_y - \bar{w}\boldsymbol{\partial}_z. \tag{4.20}$$

| $L_y$ | $N_y$ | $N_z$ | $\sigma$ |
|---|---|---|---|
| 11.0 | 234 | 121 | 0.6301 |
| 11.0 | 258 | 121 | 0.6399 |
| 11.0 | 282 | 121 | 0.6461 |
| 13.0 | 284 | 121 | 1.0660 |
| 13.0 | 313 | 121 | 1.0669 |
| 13.0 | 342 | 121 | 1.0665 |
| 15.0 | 310 | 121 | 1.0674 |
| 15.0 | 340 | 121 | 1.0684 |
| 15.0 | 371 | 121 | 1.0686 |
| 13.0 | 313 | 121 | 1.0669 |
| 13.0 | 313 | 141 | 1.1038 |
| 13.0 | 313 | 161 | 1.1222 |
| 13.0 | 313 | 181 | 1.1316 |
| 13.0 | 313 | 201 | 1.1367 |

TABLE 1. Convergence data regarding the necessary domain length and grid resolution for $Pe = 2000$, $R = 7$ and $\beta = 2$.

and

$$\boldsymbol{B} = \begin{pmatrix} \mathbf{0} & \mathbf{0} & \mathbf{0} & \mathbf{0} & \mathbf{0} \\ \mathbf{0} & \mathbf{0} & \mathbf{0} & \mathbf{0} & \mathbf{0} \\ \mathbf{0} & \mathbf{0} & \mathbf{0} & \mathbf{0} & \mathbf{0} \\ \mathbf{0} & \mathbf{0} & \mathbf{0} & \mathbf{0} & \mathbf{0} \\ \mathbf{0} & \mathbf{0} & \mathbf{0} & \mathbf{0} & \boldsymbol{I} \end{pmatrix}, \quad \boldsymbol{\phi} = \begin{pmatrix} \hat{p} \\ \hat{u} \\ \hat{v} \\ \hat{w} \\ \hat{c} \end{pmatrix}. \tag{4.21}$$

The viscosity ratio $R$ and the Péclet number $Pe$ represent the two dimensionless parameters that characterize the base flow, and the wavenumber $\beta$ reflects the perturbation wavelengths.

### 4.2. *Numerical solution*

In order to calculate the largest eigenvalues along with the corresponding eigenvectors, we employ the ARPACK package based on the Arnoldi iteration method (Lehoucq, Sorenson & Yang 1998). This iterative solver requires an external linear solver. In this context it is helpful that $\boldsymbol{A}$ is extremely sparse, with fewer than 0.2 % of the entries differing from zero. We avoid establishing the complete matrix by storing only the non-zero elements, and use a sparse direct linear solver implemented in the software package UMFPACK (Davis & Duff 1997; Davis 2003*a*). This approach differs from the one employed by Graf & Meiburg (2002) and Goyal & Meiburg (2004), who used spectral schemes for the discretization, with a non-equidistant grid in the streamwise direction. In this case the discrete derivative operators are more dense, and $\boldsymbol{A}$ has about 2 % non-zero elements. Test calculations show that the incorporation of an interpolated base flow in the stability calculations increases the necessary spatial resolution. Detailed comparisons show that for a second-order scheme, the number of grid points required for convergence is around three times that for the spectral scheme. However, because of the extremely sparse nature of the operators and coefficient matrices, it still pays off to use the lower-order method, as the overall memory and time requirements are smaller compared to the spectral approach.

We performed several checks to determine the required domain length in the streamwise direction, along with the minimum number of grid points necessary to obtain converged eigenvalues and well-resolved eigenvectors. It was found that smaller wavenumbers generally require larger domain sizes. Table 1 provides a summary of

these validation studies for a particular wavenumber, viscosity ratio and Péclet number. First, we check on the domain length and necessary resolution in the flow direction. It is evident that increasing $L_y$ beyond 13 and $N_y$ above 313 does not alter the leading eigenvalue by more than 1 %. In the bottom half of the table we similarly determine the sufficient value of $N_z$ to be 181. A minimum domain length of 10 was always maintained. In our current investigation the smallest wavenumber was $\beta = 0.25$, which required a domain of size 26. The largest grid we needed for our stability calculations was $N_y = 353$ and $N_z = 201$. Since we solve for five variables at each grid point, the matrix $\boldsymbol{A}$ is of size $(5 \times N_y \times N_z)^2$, where $N_y$ and $N_z$ are the number of grid points in the $y$- and $z$-directions, respectively. Hence, for the largest grid the matrix is of size $354,765 \times 354,765$. 50GB of memory is required to perform the stability analysis for this grid resolution, which reflects the magnitude of the calculations.

The final set of validation studies is intended to confirm that over the duration of the quasi-steady base state, the linear stability results do not depend on the specific time at which the base state is evaluated. As mentioned earlier, for $Pe = 2000$ and $R = 5$ the quasi-steady base state around the moving displacement front persists from about $t = 2.5$ to an indeterminately long time. We performed linear stability calculations at the two different times of $t = 2.5$ and 3.5, respectively, and obtained identical growth rates over the entire range of wavenumbers.

### 4.3. *Results*

We obtain dispersion relations for all combinations of $Pe$ and $R$ examined in the current study. The growth rate increases with the wavenumber, up to a particular value of $\beta$, beyond which the growth rates decrease with further increase in the wavenumber. This clear peak at an intermediate wavenumber, reflects the most unstable perturbation wavelength. Additionally, for each parameter combination there is a cutoff wavenumber, beyond which all perturbations are damped. Figure 12 provides contour plots of the eigenfunctions for all perturbation components, corresponding to the dominant wavelength mode for a particular parameter combination. The superimposition of the concentration eigenfunction in the bottom part of figure 12 shows that the instability develops centred around the tip of the moving front. The concentration perturbation lies almost entirely within the interfacial thickness of the front while the velocity components spread over a greater distance in the streamwise direction.

Figure 13 gives a physical view of the instability in the spanwise direction. The contours in figure 13($a$) reflect the wavy shape of the interface separating the two fluids, along with the perturbation velocity directional vectors in the centre-gap $(x, y)$-plane. Here, the interface contours were obtained by adding a suitable multiple of the concentration eigenfunction to the base concentration field. It can be seen that at the wave crests the interface is accelerated by the perturbation velocity, while it is being slowed down at the troughs. This stretching of the front in the direction of the flow reflects a growing instability mode. Figure 13($b$) displays the interface obtained as mentioned above together with the velocity directional vectors in the $(x, z)$-plane at a location inside the front, just behind its tip. The interface is symmetric about the centreline of the Hele-Shaw cell, as reflected by identical concentration contours on either side of the $z = 0$ line. At a certain spanwise location the front is seen to widen, while at neighbouring locations its width decreases. In summary, there are two superimposed roll-like structures which, periodically in the spanwise direction,

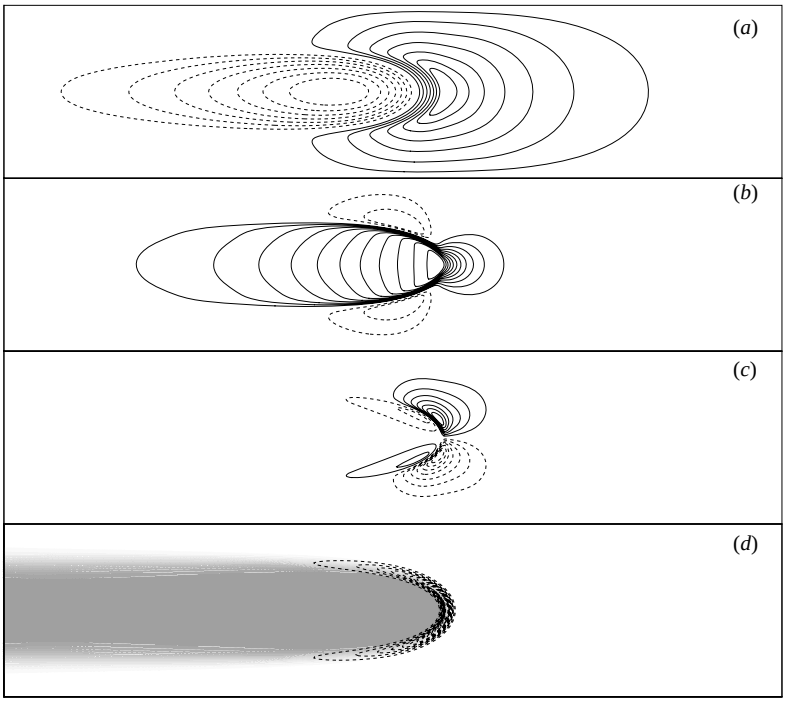


FIGURE 12. The eigenfunctions for (from top to bottom) $\hat{u}$, $\hat{v}$, $\hat{w}$ and $\hat{c}$, for $Pe = 1000$, $R = 5$ and $\beta = 2$. The concentration eigenfunction is superimposed on the base flow concentration field. It shows that the instability develops centred around the tip of the front. Solid lines denote positive values, while dashed lines indicate negative ones.

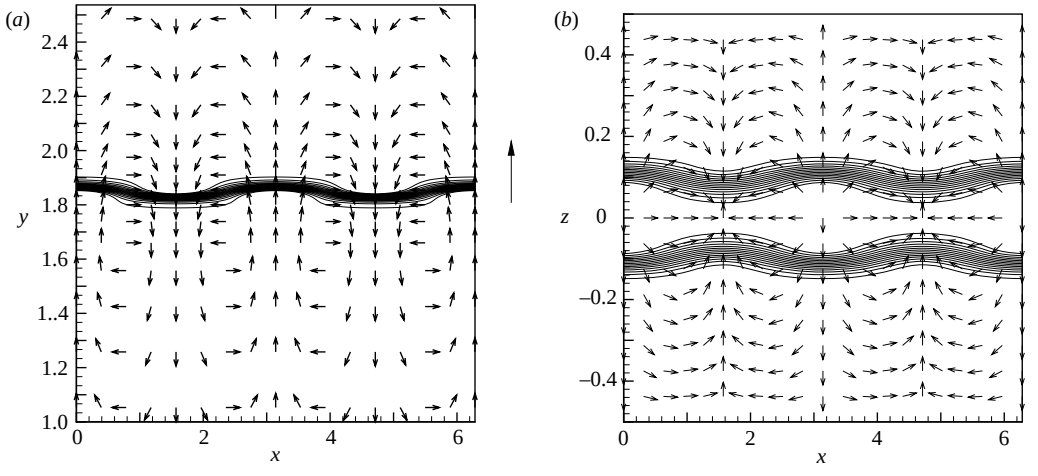


FIGURE 13. (*a*) Perturbation velocity directional vectors superimposed on the total concentration field in (*a*) the centre-gap $(x, y)$-plane, and (*b*) the $(x, z)$-plane at $y = 1.84$, just behind $y_{tip} = 1.85$. Two roll-like structures are observed which, periodically in the spanwise direction, accelerate (decelerate) and widen (narrow) the displacement front.

accelerate (decelerate) and widen (narrow) the front. A comparison of the magnitude of the perturbation vorticity from these figures shows that the primary motion is caused by the counter-rotating rolls in the $(x, y)$-plane, as the cross-gap component of

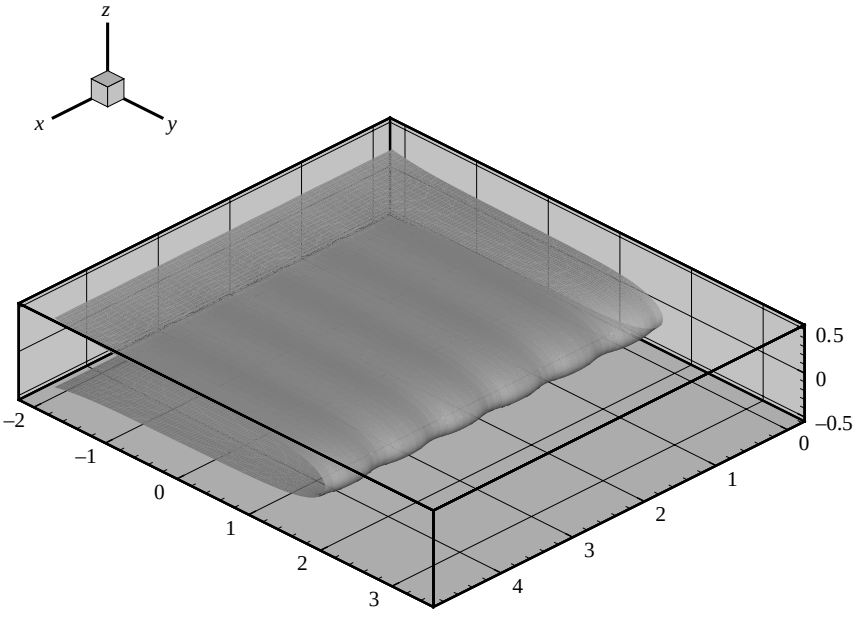


FIGURE 14. Three-dimensional view of the spanwise instability.

vorticity is much larger than the streamwise component. Figure 14 shows a qualitative three-dimensional view of the development of the instability in the spanwise direction. In order to obtain this figure, we again added a multiple of the three-dimensional perturbation concentration to the base concentration and then plotted the $c = 0.5$ contour.

In the following, we shall focus on the growth rates and wavelengths of the dominant modes for various parameters. Figure 15 displays the growth rate of the most amplified wavenumber as a function of the viscosity ratio for different Péclet numbers. An increase in the viscosity contrast is found to be uniformly destabilizing for all Péclet numbers, except a slight damping effect for $Pe = 2000$ as $R$ increases from 6 to 7. The growth rate increases monotonically with $Pe$ for $R < 5$, while at even higher viscosity ratios, larger $Pe$ values lower the growth rate, as seen in the inset of figure 15. We plot the wavenumber of the most dangerous mode and the cutoff mode with the viscosity ratio in figure 16. An increase in the viscosity contrast leads to a decrease in the dominant wavenumber for all values of $Pe$. For $Pe = 2000$, however, the wavenumber does increase very mildly, as $R$ increases form 6 to 7. With increasing $Pe$, the $\beta_{max}$ shifts towards larger wavelengths for all values of $R$. At $R = 7$, it is nearly independent of $Pe$. Even though the wavelength of the dominant mode increases with $Pe$ and $R$, the cutoff wavelength decreases with increasing values of these parameters (cf. figure 16*b*), similar to earlier findings. Figure 16 suggests that a further increase in the Péclet number will shift the most amplified mode to even lower wavenumbers, and thereby closer to the wavenumbers observed in the high-$Pe$ experiments of Paterson (1985) and Lajeunesse *et al.* (1997), which were conducted at $Pe \backsim O(10^5)$.

Darcy flows exhibit entirely different behaviour with regard to the dominant wavelengths and their growth rates, and will be discussed in detail later. The current findings are also in direct contrast to the earlier findings of Fernandez *et al.* (2002) and Graf & Meiburg (2002) for gravity-driven instabilities in a Hele-Shaw cell without

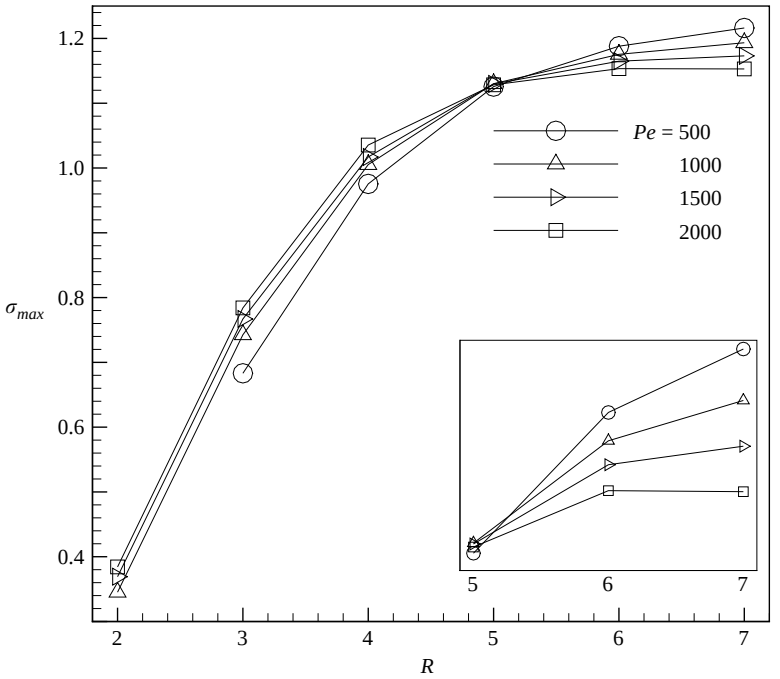


FIGURE 15. Growth rate of the most dangerous mode as a function of the viscosity ratio for different Péclet numbers. For small viscosity contrasts, higher *Pe* values are destabilizing, while for $R \geqslant 5$ the growth rates decrease with increasing *Pe*.

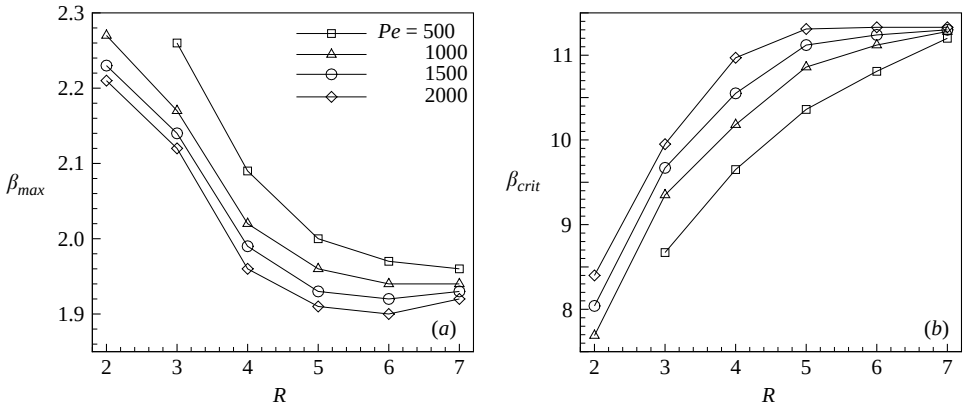


FIGURE 16. Wavenumber of (*a*) the most dangerous mode and (*b*) the cutoff mode as a function of the viscosity ratio for different *Pe*. Higher *Pe* values increase the dominant perturbation wavelength and decrease the cutoff wavelength for all *R*.

a net displacement. These authors observe a decrease in the dominant wavelength with increasing Rayleigh number, which similarly to *Pe* represents a measure of convective to diffusive transport. This seems to indicate that there is a qualitative difference between the nature of the instabilities in displacement flows *vs.* those driven by gravitational effects, at least at high *Pe*. It is not immediately obvious why an increase in *Pe* leads to longer wavelength dominant modes, or lower growth rates at higher viscosity ratios. The important length scales in the baseflow field,

besides the width of the gap, are the front thickness $d_0$ and the reduced width of the finger $\lambda$. $d_0$ decreases uniformly with $Pe$ and $R$ (cf. figure 5), while $\lambda$ decreases with $Pe$ for small values of $R$ and exhibits a reverse trend at larger viscosity contrasts (cf. figure 11). We would expect thinner and narrower fronts to be more unstable, because of stronger concentration gradients. On the other hand, Goyal & Meiburg (2004) found a stabilizing effect of decreasing interfacial thickness of the base state concentration profile on gravitationally driven instabilities in a Hele-Shaw cell. They attribute this to the two interacting length scales present in the Hele-Shaw problem, namely, the finite width of the gap and the interfacial thickness of the mixing layer. Thicker interfaces increasingly shift the eigenfunctions into the less viscous fluid at high $R$, leading to lesser damping and higher growth rates.

However, in the present case with complex interfacial shapes of the eigenfunctions and far thinner interfaces, we do not notice any significant shift of the eigenfunctions which reside almost completely within the tip of the displacement front over the entire range of $Pe$ and $R$ examined here. Further, the relatively mild damping of the growth rates with $Pe$ at high values of $R$ and also with $R$ for $Pe = 2000$, leads to very similar looking eigenfunctions. In an attempt to understand these effects, we tried to delineate the effects of the various parameters in the baseflow from those caused by the variation of $Pe$ and $R$ in the perturbation equations. Hence, we performed some stability calculations by varying $Pe$ and $R$ artificially for different baseflow configurations, in contrast to true flows where these parameters would have the same values in both the two-dimensional simulations and the linear stability analysis. This could help us distinguish and compare the relative influence of $d_0$ and $\lambda$, with that of $Pe$ and $R$ on the perturbations. These calculations showed that an increase in $Pe$ in the perturbation equations causes the eigenfunctions to become sharper and reside completely within the tip of the baseflow front, which always has a stabilizing effect. $d_0$ and $\lambda$ have a rather weak influence on the growth rates of the perturbation, though generally, thicker and wider interfaces are more stable than their thinner, narrow counterparts. As for the case of true flows, discussed earlier, we do not observe a discernible shift of the eigenfunctions into the less viscous fluid.

These observations are in contrast to the gravity-driven instability (Graf & Meiburg 2002; Goyal & Meiburg 2004), where the front thickness plays an important role in determining the growth rates. Figure 16 shows that the influence of $Pe$ on $\beta_{max}$ and $\beta_{crit}$ is very small and to a first approximation, they are practically independent of $Pe$. As demonstrated by the scaling arguments of Fernandez *et al.* (2001), it seems that the gapwidth alone sets the length scale of the viscous fingering instability, while the changes in the base state modify it only slightly.

### 4.4. *Comparison with miscible Hele-Shaw experiments*

Paterson (1985) conducted radial displacements of glycerin by water ($R \backsim 7$) at high $Pe$ numbers of $O(10^5)$. He observed a dominant wavelength of about four times the gap width. In comparison, for this value of $R$, our linear stability analysis predicts a dominant wavelength of about 3.3 gap widths, albeit at a much lower value of $Pe$ (cf. figure 16). Computational limitations prevent us from extending our analysis to values much beyond $Pe = 2000$. However, figure 16 indicates that for $R = 7$ the dominant wavelength does not vary strongly with $Pe$, at least in the $Pe$-range investigated here. Overall, there is a tendency for the dominant wavelength to increase with $Pe$, which would bring the linear stability results closer to the experimental values. In assessing the comparison, furthermore, it is to be kept in mind that the experiments were carried out in the radial configuration, as opposed to the rectilinear flow considered

in the stability analysis. In addition, the dominant wavelength in the experiments was determined during the nonlinear stage, and not during the early stage of infinitesimal perturbations. Given these limitations, the agreement between theory and experiment can be considered satisfactory.

Lajeunesse *et al.* (1997) observe a dominant wavelength of $5 \pm 1$ gap widths for their variable density, miscible displacement experiments in vertical Hele-Shaw cells at $Pe > 10^4$. They point out that this value of the dominant wavelength is rather independent of $R$ over a wide range of mobility ratios from $R \approx 1$ to $R \approx 6$. As mentioned above, it is possible that gravitational effects have an influence on the dominant wavelength. The dominant wavelength in vertical displacements with density stratification is an open question that we plan to address in more detail in the future.

Snyder & Tait (1998) conducted experiments in horizontal Hele-Shaw cells with neutrally buoyant fluids and found the dominant wavelength of the instability to be around twice the gap width. However, their data show substantial scatter across the entire range of mobility ratios, so that a precise comparison is not possible.

### 4.5. *Comparison with results obtained from Darcy's law*

Hickernell & Yortsos (1986) derived bounds for the growth of small perturbations in porous media displacements in the absence of diffusion and dispersion. Tan & Homsy (1986) treat both isotropic and highly anisotropic dispersion media in their linear stability theory based on Darcy's law. We rescale their relation corresponding to isotropic dispersion in terms of our non-dimensional parameters, using the additional facts that the flow rate is the same in both cases, and that the permeability of their porous medium is related to the gap width of the Hele-Shaw cell. The dispersion relation for a step concentration profile then reads

$$\sigma = \frac{\beta}{24Pe}\{(RPe - 12\beta) - \sqrt{144\beta^2 + 24R\beta Pe}\}. \tag{4.22}$$

In figure 17, we compare the present Stokes flow dominant mode growth rates and wavenumbers with those corresponding to (4.22) for the two lower values of $Pe$ considered here. Clearly, the dominant wavelengths and their growth rates are not captured accurately by the Darcy analysis. At the lowest values of $Pe = 500$, and $R = 3$ the growth rates are comparable while an increase in either parameter leads to a large discrepancy. We do not plot the cutoff modes from Darcy's analysis here, but mention that like the dominant wavenumber, it follows the same trend of a linear increase with the viscosity ratio and much higher values as compared to the Stokes analysis. For long waves, the Darcy analysis underpredicts the growth rate, while it overpredicts the growth of short waves. Given the obvious limitations inherent in applying Darcy's law to variable viscosity flows in Hele-Shaw cells, this finding is not unexpected, and it agrees with corresponding observations by Graf & Meiburg (2002) for gravitationally driven instabilities.

### 4.6. *Miscible vs. immiscible flow*

It is of interest to compare the influence of $Pe$ in unstable miscible displacements with that of the capillary number $Ca$ in immiscible ones. For small values of $Ca$, Park & Homsy (1984) perform asymptotic expansions in order to determine the dominant wavelength. Their results, which were confirmed by the experiments of Park, Gorell & Homsy (1984), yield much larger wavelengths than found here. Subsequently, Maxworthy (1989) compiled experimental results by several authors for the dominant wavelength over a range of $Ca$ ($10^{-3} < Ca < 30$). The data generally compare well with those of Park & Homsy (1984) and Schwartz (1986) at low capillary numbers. At

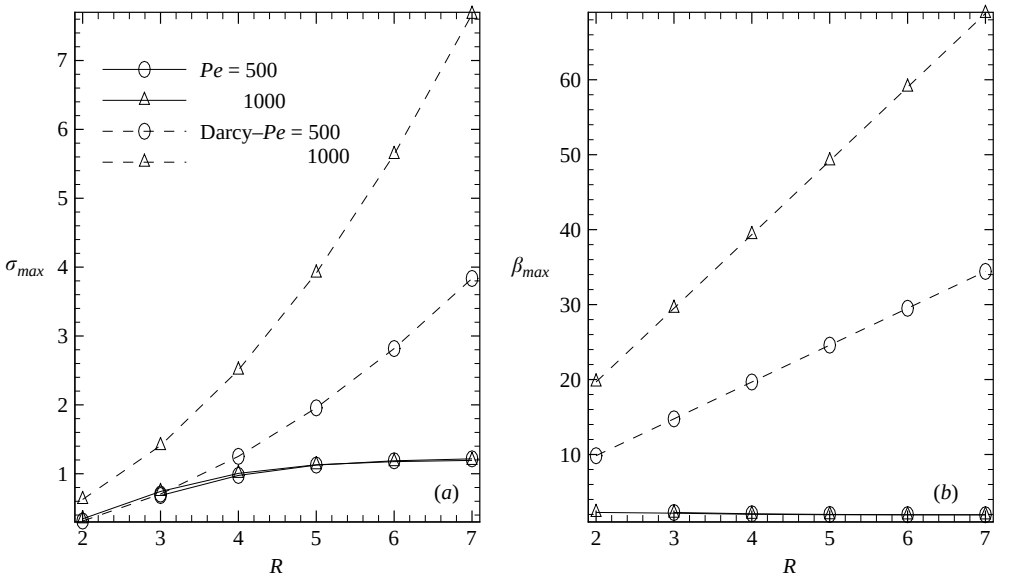


FIGURE 17. Comparison of the present Stokes flow results (solid lines) with (*a*) growth rates and (*b*) wavenumbers based on Darcy's law (dashed lines) for different Péclet numbers (Tan & Homsy 1986).

higher $Ca$ ($1 < Ca < 30$), the dominant wavelength remains fairly constant at about five times the gap width of the Hele-Shaw cell. This value is reasonably close to the dominant wavelength of about 3.3 gap widths found here for high viscosity contrasts and large $Pe$.

## 5. Discussion and conclusions

The present investigation is intended to shed light on the miscible fingering instability encountered when a less viscous fluid displaces a more viscous one in a Hele-Shaw cell. As a first step, we performed two-dimensional Stokes simulations of miscible displacements in a gap for Péclet numbers up to $10^4$ and mobility ratios up to about $10^3$, corresponding to $R = 7$. In the lower range of $Pe$ and $R$, these simulations agree closely with the earlier results of Rakotomalala *et al.* (1997). The results indicate the existence of a quasi-steady state near the tip of the front for $Pe > O(500)$ and $R > 2 - 3$.

We characterize this quasi-steady state in terms of the front thickness and its propagation velocity. The front thickness is seen to scale with $Pe^{-1/2}$, while it is only a weak function of the viscosity ratio. These findings are in agreement with corresponding observations by Chen & Meiburg (1996) for miscible displacements in capillary tubes. The nature of the viscosity–concentration relationship has a significant influence on the quasi-steady state. For the exponential relation employed throughout most of the investigation, we find that the tip velocity increases with $Pe$ for small $R$, while it decreases with $Pe$ for large $R$. In contrast, for a linear viscosity–concentration relationship, the tip velocity is seen to increase with $Pe$ for all viscosity ratios. The simulation results suggest that in the limit of large $Pe$ and $R$, the width and tip velocity of the front would asymptote to the same values as the immiscible counterpart studied by Reinelt & Saffman (1985) for large $Ca$.

In a second step, we examine the stability of this quasi-steady front to spanwise perturbations. For all *Pe*, the maximum growth rate is found to increase monotonically with *R*. At the largest value of *Pe*, however, the maximum growth rate is observed at $R = 6$ and a slight damping occurs with further increase in the viscosity contrast. The influence of *Pe* on the growth of the instability is non-uniform. For mild viscosity contrasts, a larger *Pe* is found to be destabilizing, while for large viscosity contrasts, an increase in *Pe* has a slightly stabilizing influence. We performed artificial calculations to try and understand these effects. These did show that increasing *Pe* in the perturbation equations surprisingly leads to a damping of the instability, while the baseflow front thickness and width tend to modify the growth rates and wavelengths only slightly. We did not observe a shift in the eigenfunctions for higher *R*, similar to our earlier investigation of gravity-driven instabilities in Hele-Shaw cells (Goyal & Meiburg 2004). In that situation, the competing influence of the two length scales that enter the problem, namely, the interface thickness and the gap width of the Hele-Shaw cell, led to higher growth rates for thicker interfaces at large viscosity contrasts. Apparently, the gap width of the cell alone sets the length scale of the instability in the present case, and both *R* and *Pe* have a relatively weak effect on the dominant wavelength.

Many of the above effects are in stark contrast to observations based on Darcy's law, which find higher values of *Pe* and *R* to be uniformly destabilizing, and to result in shorter instability wavelengths. The less complex behaviour of Darcy flows originates from the presence of only one length scale in the problem, namely, the initial interfacial thickness, while the added influence of the gap width causes much more complex behaviour in Hele-Shaw flows.

A close inspection of the instability eigenfunction reveals the presence of two sets of counter-rotating roll-like structures, with axes aligned in the cross-gap and in the streamwise directions. The former lead to the periodic, in the spanwise direction, acceleration and deceleration of the front, while the latter result in the thickening and thinning of the front. These roll-like structures are aligned in such a way that the front thickens where it speeds up, and thins where it slows down.

While detailed experimental data are not available for the growth rate of the fingering instability, such data do exist for the dominant wavelength. Compared to the experimental observations by Paterson (1985), our linear stability results predict a somewhat lower most amplified wavelength. There may be several reasons for this discrepancy. First, Paterson's observations were made in radial displacements, while our analysis considers rectilinear flows. Secondly, his data may have been collected during a stage of the flow that was already influenced by nonlinear effects. Finally, and perhaps most importantly, his experiments were conducted at *Pe* of $O(10^5)$, whereas the present results are limited to *Pe* no larger than $10^4$. The linear stability analysis shows that increasing *Pe* values generally lead to larger dominant wavelengths, which does suggest that better agreement would be obtained if we were able to conduct the analysis at the values of *Pe* employed in the experiments. Similarly, the wavelengths predicted by the present linear stability analysis are somewhat smaller than the experimental observations by Lajeunesse *et al.* (1997). However, it is to be kept in mind that these authors consider vertical displacements in the presence of density differences, which may well affect the dominant wavelength.

Finally, the present investigation comments on similarities and discrepancies between the role of *Pe* in miscible displacements, and that of *Ca* in immiscible ones. For immiscible displacements at infinite viscosity ratio, the theoretical analysis by Park & Homsy (1984) and the compilation of experimental data by Maxworthy

(1989) show that for low $Ca$, the wavelength of the most dangerous mode scales as $Ca^{-1/2}$, while for large $Ca$, a dominant wavelength of about five times the gap width emerges. On the other hand, the present results show that for large $R$, the dominant wavelength is largely independent of $Pe$ and has a value of about 3.3 gap widths. For small viscosity contrasts, the wavelength is seen to increase with $Pe$. These observations indicate the limitations of the $Pe - Ca$ analogy.

Possible extensions of the current investigation will address the effects of density stratification in a gravitational field. In particular, it will be interesting to quantify the modification of the most dangerous wavelength and the associated growth rate by density effects, as this may aid in the comparison with the experimental data discussed above. Furthermore, an extension of the present study into the nonlinear regime promises to provide new insight. Specifically, it will be interesting to compare the merging, splitting and shielding processes observed in three-dimensional Stokes simulations with their Darcy counterparts. Efforts in these directions are currently underway.

We would like to thank Dr L. Talon for several helpful discussions. Support for this research was received from the NASA Microgravity and NSF/ITR programs, as well as from the Department of Energy, and through an NSF equipment grant.

## REFERENCES

Chen, C. & Meiburg, E. 1996 Miscible displacements in capillary tubes. Part 2. Numerical simulations. *J. Fluid Mech.* **326**, 57–90.

Chen, C. & Meiburg, E. 1998 Miscible porous media displacements in the quarter five-spot configuration. Part 1. The homogeneous case. *J. Fluid Mech.* **371**, 233–268.

Chouke, R., Meurs, P. & Poel, C. V. 1959 The instability of slow, immiscible, viscous liquid–liquid displacements in permeable media. *Trans. AIME* **216**, 188–194.

Cox, B. 1962 On driving a viscous fluid out of a tube. *J. Fluid Mech.* **14**, 81–96.

Davis, T. 2003*a* Algorithm 8xx:umfpack v4.1, an unsymmetric-pattern multifrontal method with a column pre-ordering strategy. *Tech. Rep.* Department of Computer and Information Science and Engineering, University of Florida.

Davis, T. 2003*b* *UMFPACK Version 4.1 User Guide*. Department of Computer and Information Science and Engineering, University of Florida.

Davis, T. & Duff, I. 1997 An unsymmetric-pattern multifrontal method for sparse lu factorization. *SIAM J. Matrix Anal. Applics.* **18**, 140–158.

Fernandez, J., Kurowski, P., Limat, L. & Petitjeans, P. 2001 Wavelength selection of fingering instability inside Hele-Shaw cells. *Phys. Fluids* **13**, 3120–3125.

Fernandez, J., Kurowski, P., Petitjeans, P. & Meiburg, E. 2002 Density-driven, unstable flows of miscible fluids in a Hele-Shaw cell. *J. Fluid Mech.* **451**, 239–260.

Fletcher, C. 1990 *Computational Techniques for Fluid Dynamics*, vol. 2. Springer.

Goyal, N. & Meiburg, E. 2004 Unstable density stratification of miscible fluids in a vertical Hele-Shaw cell: influence of variable viscosity on the linear stability. *J. Fluid Mech.* **516**, 211–238.

Graf, F. & Meiburg, E. 2002 Density-driven instabilities of miscible fluids in a Hele-Shaw cell: linear stability analysis of the three-dimensional Stokes equations. *J. Fluid Mech.* **451**, 261–282.

Hickernell, F. & Yortsos, Y. 1986 Linear stability of miscible displacement processes in porous media in the absence of dispersion. *Stud. Appl. Maths* **74**, 93–115.

Hill, S. 1952 Channeling in packed columns. *Chem. Engng. Sci.* **1**, 247.

Homsy, G. 1987 Viscous fingering in porous media. *Annu. Rev. Fluid Mech.* **19**, 271.

Lajeunesse, E., Martin, J., Rakotomalala, N. & Salin, D. 1997 3D instability of miscible displacement in a Hele-Shaw cell. *Phys. Rev. Lett.* **79**, 5254–5257.

Lajeunesse, E., Martin, J., Rakotomalala, N., Salin, D. & Yortsos, Y. 1999 Miscible displacement in a Hele-Shaw cell at high rates. *J. Fluid Mech.* **398**, 299–319.

Lehoucq, R., Sorenson, D. & Yang, C. 1998 *ARPACK USERS GUIDE : Solution of Large Scale Eigenvalue Problems with Implicitly Restarted Arnoldi Methods*. SIAM Philadelphia.

Lele, S. 1992 Compact finite difference schemes with spectral-like resolution. *J. Comput. Phys.* **103**, 16–42.

Manickam, O. & Homsy, G. 1995 Fingering instabilities in vertical miscisble displacement flows in porous media. *J. Fluid Mech.* **288**, 75–102.

Maxworthy, T. 1989 Experimental study of interface instability in a Hele-Shaw cell. *Phys. Rev.* A **39**, 5863–5867.

Panton, R. L. 1984 *Incompressible Flow*, vol. 2. John Wiley.

Park, C., Gorell, S. & Homsy, G. 1984 Two-phase displacements in Hele-Shaw cells: experiments on viscously driven instabilities. *J. Fluid Mech.* **141**, 275–287.

Park, C. & Homsy, G. 1984 Two-phase displacements in Hele-Shaw cells: theory. *J. Fluid Mech.* **139**, 291–308.

Paterson, L. 1985 Fingering with miscible fluids in a Hele-Shaw cell. *Phys. Fluids* **28**, 26–30.

Petitjeans, P., Chen, C., Meiburg, E. & Maxworthy, T. 1999 Miscible quarter five-spot displacements in a Hele-Shaw cell and the role of flow-induced dispersion. *Phys. Fluids* **11**, 1705–1716.

Petitjeans, P. & Maxworthy, T. 1996 Miscible displacements in capillary tubes. Part 1. Experiments. *J. Fluid Mech.* **326**, 37–56.

Rakotomalala, N., Salin, D. & Watzky, P. 1997 Miscible displacement between two parallel plates: BGK lattice gas simulations. *J. Fluid Mech.* **338**, 277–297.

Reinelt, D. & Saffman, P. 1985 The penetration of a finger into a viscous fluid in a channel and tube. *SIAM J. Sci. Stat. Comput.* **6**, 542–561.

Ruith, M. & Meiburg, E. 2000 Miscible rectilinear displacements with gravity override. Part 1. Homogeneous porous medium. *J. Fluid Mech.* **420**, 225–257.

Saffman, P. & Taylor, G. 1958 The penetration of a fluid into a porous medium or a Hele-Shaw cell containing a more viscous fluid. *Proc. R. Soc. Lond.* A **245**, 312–329.

Schwartz, L. 1986 Stability of Hele-Shaw flows: the wetting layer effect. *Phys. Fluids* **29**, 3086–3088.

Snyder, D. & Tait, S. 1998 A flow-front instability in viscous gravity currents. *J. Fluid Mech.* **369**, 1–21.

Tan, C. & Homsy, G. 1986 Stability of miscible displacements in porous media: rectilinear flow. *Phys. Fluids* **29**, 3549–3556.

Tan, C. & Homsy, G. 1987 Stability of miscible displacements: radial source flow. *J. Fluid Mech.* **30**, 1239–1245.

Taylor, G. 1953 Dispersion of soluble matter in a solvent flowing slowly through a tube. *Proc. R. Soc. Lond.* A **219**, 186.

Taylor, G. 1961 Deposition of a viscous fluid on the wall of a tube. *J. Fluid Mech.* **10**, 161–165.

Vanaparthy, S., Meiburg, E. & Wilhelm, D. 2003 Density-driven instabilities of miscible fluids in a capillary tube: linear stability analysis. *J. Fluid Mech.* **497**, 99–121.

Wooding, R. 1969 Growth of fingers at an unstable diffusing interface in a porous medium or Hele-Shaw cell. *J. Fluid Mech.* **39**, 477–495.

Wray, A. 1991 Minimal storage time advancement schemes for spectral methods. Preprint.

Yang, Z. & Yortsos, Y. 1997 Asymptotic solutions of miscible displacements in geometries of large aspect ratio. *Phys. Fluids* **9**, 286–298.

Yortsos, Y. 1987 Stability of displacement processes in porous media in radial flow geometries. *Phys. Fluids* **30**, 2928–2935.

Yortsos, Y. & Zeybek, M. 1988 Dispersion driven instability in miscible displacement in porous media. *Phys. Fluids* **31**, 3511–3518.